Dan Wang¹

Western Digital Corp, San Jose, CA 95119 email: danwang1230@gmail.com

Xu Chen

Department of Mechanical Engineering, University of Washington, Seattle, WA 98195 email: chx@uw.edu

Multi-track Melt Pool Width Modelling in Powder Bed Fusion Additive Manufacturing

While powder bed fusion (PBF) additive manufacturing offers many advantages and exciting applications, its broader adoption is hindered by issues with reliability and variations during the manufacturing process. To address this, researchers have identified the importance of using both finite element modeling and control-oriented modeling to predict and improve the quality of printed parts. In this paper, we propose a novel control-oriented multi-track melt pool width model that utilizes the superposition principle to account for the complex thermal interactions that occur during PBF. We validate the effectiveness of the model by applying a finite element model of the thermal fields in PBF.

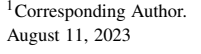
Keywords: modeling, control implementation, power bed fusion, additive manufacturing

1 Introduction

Additive manufacturing (AM) differs from conventional subtractive machining as it creates a part by adding material layer by layer, directly from a digital model. Powder bed fusion (PBF) is a specific AM technique that uses high-precision lasers or electron beams as the energy source to fuse polymeric or metallic powder materials together. While PBF has revolutionized the fabrication of complex parts, there are still challenges to its wider adoption. These challenges include issues with reliability and inprocess variations caused by uncertain laser-material interactions, environmental vibrations, powder recycling, imperfect interactions of mechanical components, and the recursive thermal histories of materials [1–5].

In PBF, a typical part is built from thousands of thin layers, as shown in Fig. 1. Each layer is created by regulating the energy beam to follow trajectories predetermined in a slicing process based on the part geometry. Once a layer is finished printing, a new thin layer of powder is spread on top, and the process repeats. Modeling this complex dynamic system (Fig. 1) is crucial for understanding and controlling PBF and related techniques. Researchers use finite element modeling to explore energy deposition mechanisms, and control-oriented modeling to build mathematical models that can regulate in-process variations. For instance, [1,6–8] adopt finite element modeling to investigate the effects of various scan configurations on the thermal fields of powder bed, the geometries of melt pool, and the mechanical properties of printed parts. In control-oriented modeling, [9-12] employ the low-order system models and further build the nonlinear submodels to cover more process dynamics. Based on these models, subsequent control algorithms such as PID control [13], sliding mode control [11], predictive control [9], repetitive control [2,14], iterative learningbased control [15], and iterative simulation-based control [4,16] have proven effective in improving the dimensional accuracy of printed parts.

This paper presents a novel approach to modeling and examining PBF by combining finite element modeling and control-oriented modeling. Firstly, we develop a finite element mode (FEM) to look into the intricate thermal interactions that occur during the PBF process. The FEM then serves as a simulation platform for gathering data and identifying parameters for the proposed modeling schemes. In contrast to the typically used low-order system models, we develop a physics-based analytical model for control-



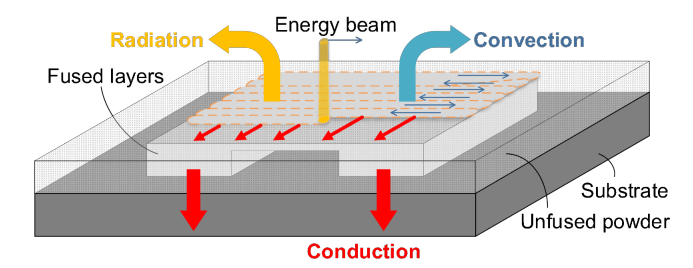


Fig. 1 Schematic of heat transfer in PBF

oriented modeling that accounts for the complex dynamic behavior of melt pool width during multi-track PBF process. The proposed control-oriented multi-track model is formulated by applying superposition to a single-track model derived from the Rosenthal equation, with melt pool width as the output. We validate the accuracy of the multi-track melt pool width model using FEM and demonstrate that the developed model can effectively represent the key characteristics of the convoluted multi-track PBF process.

The remainder of this paper is structured as follows. In Section 2, we build the FEM of the thermal fields in PBF. Section 3 explores the preliminary physics related to melt pool width. Section 4 develops and analyzes the primary multi-track melt pool width model. Finally, Section 5 concludes the paper.

2 FEM of Thermal Fields in PBF

In this section, we develop and refine an FEM to simulate the thermal fields in PBF. The FEM accounts for surface convection, surface radiation, conduction, and latent heat of fusion. To maintain computational efficiency and without compromising generality, we exclude the effects of evaporation, fluid flow, and Marangoni force when constructing the FEM using COMSOL Multiphysics 5.3a software. The governing equation for the conduction heat flow is

$$\rho c_p \frac{dT(x, y, z, t)}{dt} = \nabla \cdot (k \nabla T(x, y, z, t)) + q_s, \qquad (1)$$

where T is the temperature distribution, k the thermal conductivity, c_p the specific heat capacity, ρ the effective density, and q_s the rate of local internal energy generated per unit volume [17].

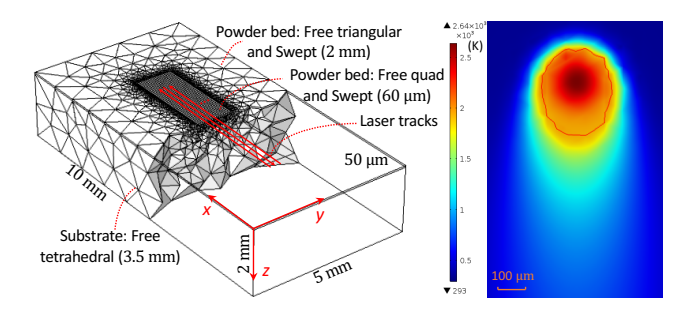


Fig. 2 Left: powder bed and substrate with selective meshing scheme. Right: surface temperature distribution at t = 0.14 s. The lined isotherm indicates $T = T_m$.

In this study, we assume a uniform distribution of the initial temperature $T(x, y, z, 0) = T_0$. When the substrate (left plot of Fig. 2) is designed to be large enough compared to the heat affected zone, one boundary condition is established by assuming the bottom of the substrate $(z = h_b)$ has no heat loss: $-k \frac{\partial T}{\partial z}\Big|_{z=h_b} = 0$. The other boundary condition considers surface conduction, convection, and radiation:

$$-k \frac{\partial T}{\partial z}\bigg|_{z=0} = -Q + h_c(T - T_0) + \varepsilon \sigma_B(T^4 - T_0^4), \tag{2}$$

where Q is the input heat flux, h_c the convection heat transfer coefficient, ε the emissivity, and σ_B the Stefan-Boltzmann constant. Here, we assume Q has a Gaussian laser beam profile: $Q \approx \frac{2q}{\pi R^2} \mathrm{e}^{-\frac{2r^2}{R^2}}$, where q is the laser power, R the effective laser beam radius, and r the radial distance from a certain point to the center of the laser spot.

We employ temperature-dependent thermal properties k, c_p , and ρ for both solid and liquid materials. Then, we calculate the thermal properties of the powder material based on the porosity of the solid material. To account for the latent heat of fusion, we introduce the effective heat capacity. The left plot of Fig. 2 displays the bidirectional scan strategy and the built geometry blocks that consist of a substrate and a thin layer of powder bed. The right plot of Fig. 2 illustrates the simulated surface temperature profile at 0.14 s, where the isotherm of $T = T_m$ depicts the melt pool geometry and T_m is the melting point. For more information regarding the thermal properties, process parameters, and meshing scheme utilized in this FEM, please refer to [4], where it has been experimentally validated.

The developed FEM functions as a simulation platform for predicting the thermal fields of the powder bed throughout the multitrack PBF process. The finite element results are shown in Fig. 3, as well as in the top plots of Figs. 6 and 8. We observe that the start of each track has larger melt pool widths than the rest of the track. This is because in bidirectional scanning, when the energy beam approaches the end of one track, the large latent heat does not have enough time to dissipate out before the next track starts. Later on we will use the data (e.g., melt pool width) generated from the FEM to identify and verify the proposed analytical model. Specifically, we obtain the melt pool width from the FEM-predicted temperature distribution by searching the isotherm of $T = T_m$ for the maximum width.

3 Preliminaries

When a moving point laser source is acting on a large thick plate, the analytical solution of (1) in the steady state is the Rosenthal equation [17]:

$$T(\xi, y, z) = T_0 + T_r,$$
 (3)

$$T_r = \frac{q}{2\pi kr} e^{-\frac{u_X(r+\xi)}{2\kappa}},\tag{4}$$

where (ξ, y, z) is a coordinate system attached to the moving source, u_x the scan speed, $r = \sqrt{\xi^2 + y^2 + z^2}$, and $\kappa = k/(\rho c_p)$.

The derivation of the Rosenthal equation involves making certain assumptions and simplifications. Firstly, the material's physical coefficients such as k, ρ , and c_p are assumed to be independent of temperature. The use of average values of these coefficients provides a reasonable approximation and enables a closed-form solution to be obtained. Secondly, the internal heat generation is neglected, i.e., $q_s = 0$. Thirdly, the workpiece material is assumed to be homogeneous and isotropic. Additionally, when the powder bed is processed long enough, a Quasistationary state is presumed to be reached, that is, the temperature undergoes no change with time in the moving coordinate system (ξ, y, z) . Moreover, a point heat source is used instead of a Gaussian distribution. Lastly, the effect of latent heat of fusion is considered negligible since the absorbed latent heat evolves later on.

From the Rosenthal equation in (3), the analytical expression of the steady-state melt pool width w for a single track is derived in [18] and further in [4]:

$$q = \pi k (T_m - T_0) w + e \pi \rho c_p (T_m - T_0) u_x w^2 / 8.$$
 (5)

Assumptions in deriving (5) include:

- $-\frac{\ln(r^*V)}{r^*M} \approx 0$, where $M = \frac{u_x}{2\kappa}$, $V = \frac{2\pi k(T_m T_0)}{q}$, and r^* represents the value of r at the melt pool width.
- $r^*M \gg 1$.
- The approximation of q is improved by including the zerospeed power, that is, the first term on the right hand side of (5).

The assumptions hold reasonably well for all alloys except AlSi10Mg under typical PBF configurations [18].

4 Multi-track Melt Pool Width Model

Melt pool width is a crucial parameter for monitoring part properties during PBF manufacturing. Maintaining a user-defined reference value for melt pool width is essential to achieving uniform part quality [19]. To fulfill this requirement, we present a novel analytical model that emulates the dynamic behavior of melt pool width during the multi-track PBF process. The application of this multi-track melt pool width model can aid in developing control algorithms that mitigate process variations and ensure consistent part quality. In this section, we implement the superposition principle to model the evolution of the multi-track melt pool width, based on the single track expression in (5). The key idea is that the cumulative thermal effect of previous tracks on the current track is reflected on the increasing initial temperature T_0 .

To explain the proposed analytical model in detail, we provide a step-by-step procedure below. The melt pool width of the first track w_1 can be directly calculated by (5) with $T_0 = T_{01} = T_{amb}$, where T_{01} indicates the initial temperature of every sample on the first track and equals the ambient temperature T_{amb} . Parameters q, u_x , k, ρ , and c_p are set to be constant. When the laser point reaches the end of the first track, for every sample on the second track as shown in Fig. 4, $\xi = (n-1)u_xt_s$, y = h, and z = 0, where n is the sample number, t_s the sampling time, and h the hatch spacing. Furthermore, we have $T_1(\xi,h,0) = T_{01}(N) + T_r(n)$ from (3), where T_1 is the temperature distribution of the laser point at the track end and N is the total number of samples per track. Here, $T_{01}(N)$ indicates the initial temperature of the last sample at the first track. The residual thermal effect of the first track on the second track are reflected on the initial temperature of every



sample on the second track: $T_{02}(n) = T_1(\xi, h, 0) = T_{01}(N) + T_r(n)$. Then with $T_0 = T_{02}$, we can calculate the melt pool width of the second track $w_2(n)$ from (5). Similarly, for the *i*-th track, we have $T_{0i}(n) = T_{0(i-1)}(N) + T_r(n)$, and the melt pool width $w_i(n)$ is the solution of (5) with $T_0 = T_{0i}$.

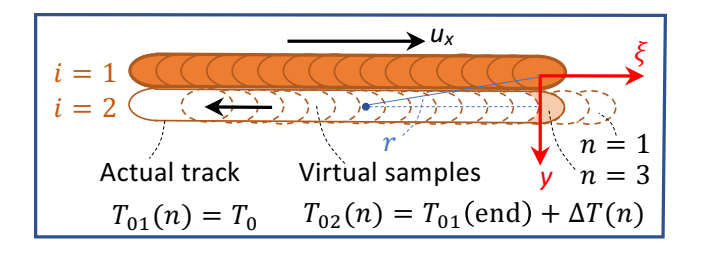
For an individual track, we notice that the melt pool width reaches its peak value a few samples after the track start, specifically at $n=n_p$. For example, $n_p=3$ in Fig. 3. On the other hand, from the analytical multi-track model, the melt pool width reaches its peak value at the track start since n=1, $\xi=(n-1)u_xt_s=0$, T_r in (4) peaks, and then T_{0i} peaks. To address the mismatch, we make an adaptation to the proposed model by shifting the virtual laser spots out by n_p-1 samples (see Fig. 5) and introducing a tuning parameter β for the first n_p-1 samples (as in Algorithm 1). Furthermore, to add more design flexibility, we reformulate T_{0i} as $T_{0i}(n)=T_{0(i-1)}(N)+T_r(n)/\alpha$ by introducing another tuning parameter α . Algorithm 1 outlines the fundamental steps of the proposed analytical model for predicting the melt pool width during the multi-track PBF process.

Algorithm 1 Multi-track melt pool width modeling

Require: number of tracks M, number of samples per track N, laser power q, scan speed u_x , melting point T_m , ambient temperature T_{amb} , sampling time t_s , hatch spacing h, thermal properties k, ρ , c_p , sample shift n_p , and tuning parameters α , β

```
1: i \leftarrow 1
2: T_{01} \leftarrow T_{amb}
 3: while i \le M do
         n \leftarrow 1
 4:
         while n \le N do
5:
 6:
              if n < n_D then
 7:
                   \xi = \beta (n - n_p) u_X t_S
 8:
 9:
                   \xi = (n - n_p)u_x t_s
10:
              end if
              r=\sqrt{h^2+\xi^2}
11:
              Calculate T_r(n) from (4)
12:
              T_{0i}(n) = T_{0(i-1)}(N) + T_r(n)/\alpha
13:
14:
              Calculate w_i(n) by (5) with T_0 = T_{0i}
              n \leftarrow n + 1
15.
         end while
16:
17:
         i \leftarrow i + 1
18: end while
```

We employ the FEM built in Section 2 to simulate the evolution of the melt pool width among multiple tracks. Using the ten-track FEM data in Fig. 6, we identify the parameters in the proposed multi-rack melt pool width model as $n_p = 3$, $\alpha = 20.8$, and $\beta = 0.5$. The other parameter values can be found in table 1. Fig. 7 shows



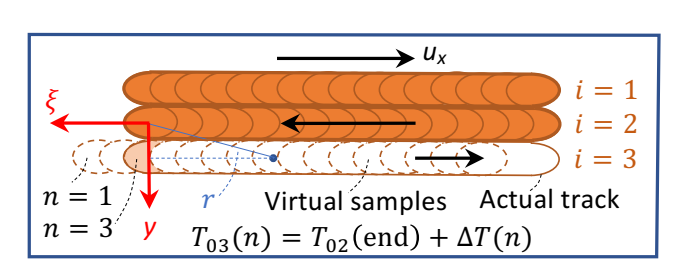


Fig. 5 After shift: illustration of initial temperature computation

i = 1 i = 2Act

 T_0

n = 1 n = 3

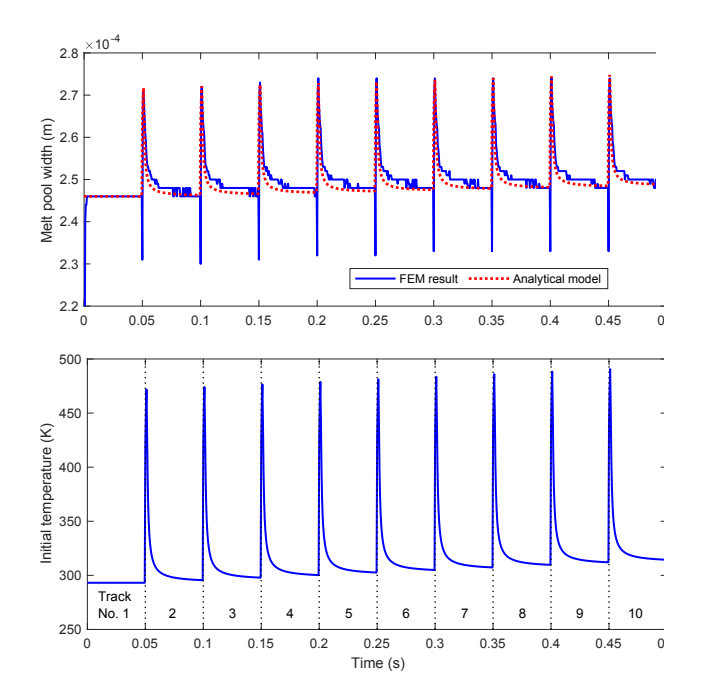


Fig. 6 Ten tracks: Top: melt pool width from analytical model and FEM. Bottom: analytical T_{0i}

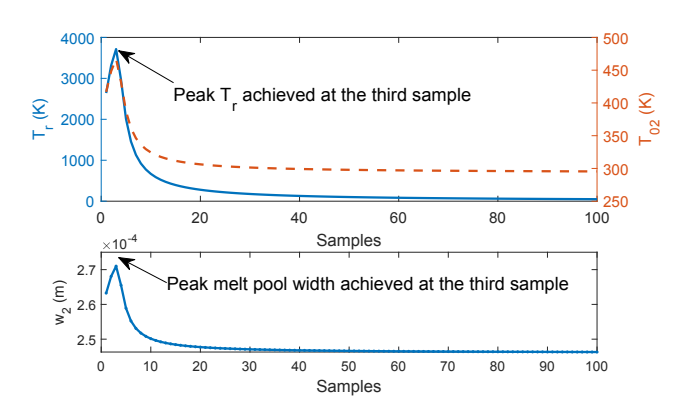


Fig. 7 Identified T_r , T_{02} , and w_2 after shift

the resulted T_r , T_{02} , and w_2 , where the analytical melt pool width peaks at the third sample after the shift. Furthermore, we compare in Fig. 8 the twenty-track melt pool results from the identified analytical model and the FEM. From the top plots of Figs. 6 and 8, we can tell that the proposed multi-track model can effectively capture the spikes at the start of each track. Moreover, the model can catch the increasing trend of the melt pool width as the track number increases. This is due to the fact that the initial temperature profile T_{0i} increases with the track number, as shown in the bottom plots of Figs. 6 and 8. Overall, the proposed model's melt pool width results closely match those of the FEM, with a difference of 5 μm. In addition, compared to FEM, the proposed model reduces the computational burden to a bare minimum. When modeling the 10-track PBF process as in Fig. 6, it takes 4.5 hours using FEM [4] and only seconds using the proposed multi-track melt pool width model. Although the FEM has been experimentally validated in [4], our future endeavors will involve further verification of the proposed model through the PBF experiments directly.

5 Conclusion

In this paper, we present a comprehensive approach to analyze the melt pool width during the multi-track powder bed fusion (PBF)

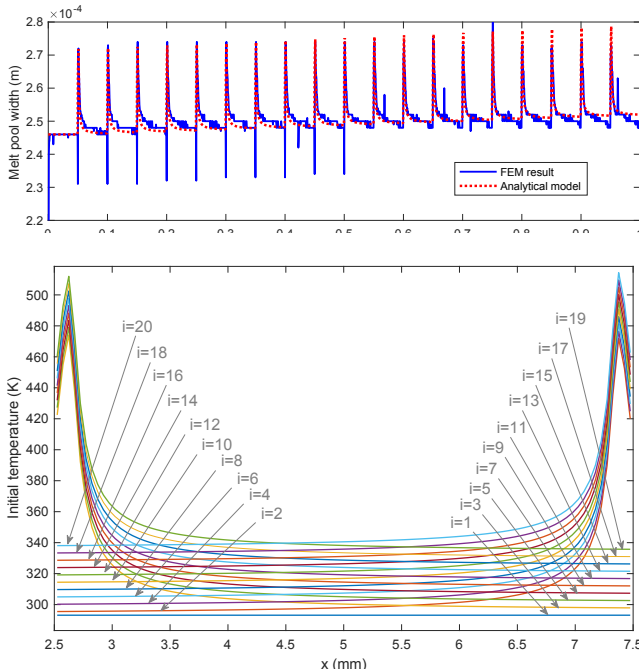


Fig. 8 Twenty tracks: Top: melt pool width from analytical model and FEM. Bottom: analytical T_{0i}

process. First, we construct a finite element model (FEM) to simulate the thermal fields of PBF. Next, we develop a multi-track analytical model by applying the superposition principle to a single-track melt pool width model derived from the Rosenthal equation. Based on the FEM data, we identify the parameters and validate the effectiveness of the proposed model. The results demonstrate that the proposed analytical model can effectively catching the complex dynamics of melt pool width that occur during the multi-track PBF process.

Acknowledgment

This work is supported by the National Science Foundation under Award No. 1953155.

References

- Liao, S., Golgoon, A., Mozaffar, M., and Cao, J., 2023, "Efficient GPUaccelerated thermomechanical solver for residual stress prediction in additive manufacturing," Computational Mechanics, pp. 1–15.
- [2] Wang, D. and Chen, X., 2018, "A multirate fractional-order repetitive control for laser-based additive manufacturing," Control Engineering Practice, 77, pp. 41–51.
- [3] Bennett, J., Webster, S., Byers, J., Johnson, O., Wolff, S., Ehmann, K., and Cao, J., 2022, "Powder-borne porosity in directed energy deposition," Journal of Manufacturing Processes, 80, pp. 69–74.
- [4] Wang, D. and Chen, X., 2021, "Closed-loop high-fidelity simulation integrating finite element modeling with feedback controls in additive manufacturing," Journal of Dynamic Systems, Measurement, and Control, 143(2).

Table 1 Parameter values

Name	Symbol	Value
Laser power	q	60 W
Scan speed	u_x	100 mm/s
Melting point	T_m	1923.15 K
Sampling time	t_{S}	0.5 ms
Ambient Temp.	T_{amb}	293.15 K
No. of samples per track	N	100
Hatch spacing	h	60 μm
Thermal properties	k, ρ, c_p	[12]

- [5] Schwalbach, E. J., Donegan, S. P., Chapman, M. G., Chaput, K. J., and Groeber, M. A., 2019, "A discrete source model of powder bed fusion additive manufacturing thermal history," Additive Manufacturing, 25, pp. 485–498.
 [6] Masoomi, M., Thompson, S. M., and Shamsaei, N., 2017, "Laser powder bed
- [6] Masoomi, M., Thompson, S. M., and Shamsaei, N., 2017, "Laser powder bed fusion of Ti-6Al-4V parts: Thermal modeling and mechanical implications," International Journal of Machine Tools and Manufacture, 118, pp. 73–90.
- [7] Ren, Y. and Wang, Q., 2023, "A finite difference method for fast prediction and control of part-scale temperature evolution in laser powder bed fusion," Journal of Manufacturing Processes, 93, pp. 299–314.
- [8] Foroozmehr, A., Badrossamay, M., Foroozmehr, E., et al., 2016, "Finite element simulation of selective laser melting process considering optical penetration depth of laser in powder bed," Materials & Design, 89, pp. 255–263.
- [9] Song, L. and Mazumder, J., 2011, "Feedback control of melt pool temperature during laser cladding process," IEEE Transactions on Control Systems Technology, 19(6), pp. 1349–1356.
- [10] Cao, X. and Ayalew, B., 2015, "Control-oriented mimo modeling of laser-aided powder deposition processes," *American Control Conference (ACC)*, 2015, IEEE, pp. 3637–3642.
- [11] Fathi, A., Khajepour, A., Durali, M., and Toyserkani, E., 2008, "Geometry control of the deposited layer in a nonplanar laser cladding process using a variable structure controller," Journal of manufacturing science and engineering, 130(3), p. 031003.
- [12] Wang, D., Zhao, X., and Chen, X., 2021, "New Hammerstein modeling and

- analysis for controlling melt pool width in powder bed fusion additive manufacturing," ASME Letters in Dynamic Systems and Control, 1(3).
- [13] Hofman, J., Pathiraj, B., Van Dijk, J., de Lange, D., and Meijer, J., 2012, "A camera based feedback control strategy for the laser cladding process," Journal of Materials Processing Technology, 212(11), pp. 2455–2462.
- [14] Wang, D., Jiang, T., and Chen, X., 2021, "Control-oriented modeling and repetitive control in in-layer and cross-layer thermal interactions in selective laser sintering," ASME Letters in Dynamic Systems and Control, 1(1), p. 011003.
- [15] Tang, L. and Landers, R. G., 2011, "Layer-to-layer height control for laser metal deposition process," Journal of Manufacturing Science and Engineering, 133(2), p. 021009.
- [16] Irwin, J. E., Wang, Q., Michaleris, P. P., Nassar, A. R., Ren, Y., and Stutzman, C. B., 2021, "Iterative simulation-based techniques for control of laser powder bed fusion additive manufacturing," Additive Manufacturing, 46, p. 102078.
- [17] Kannatey-Asibu Jr, E., 2009, Principles of laser materials processing, Vol. 4, John Wiley & Sons.
- [18] Tang, M., Pistorius, P. C., and Beuth, J. L., 2017, "Prediction of lack-of-fusion porosity for powder bed fusion," Additive Manufacturing, 14, pp. 39–48.
- [19] Chen, X., Jiang, T., Wang, D., and Xiao, H., 2018, "Realtime control-oriented modeling and disturbance parameterization for smart and reliable powder bed fusion additive manufacturing," Annual International Solid Freeform Fabrication Symposium-An Additive Manufacturing Conference.

List of Figures

1	Schematic of heat transfer in PBF	1
2	Left: powder bed and substrate with selective meshing scheme. Right: surface temperature distribution at $t = 0.14$ s.	
	The lined isotherm indicates $T = T_m$.	2
3	FEM result: surface temperature distributions showing melt pool width evolution	3
4	Illustration of initial temperature computation	3
5	After shift: illustration of initial temperature computation	3
6	Ten tracks: Top: melt pool width from analytical model and FEM. Bottom: analytical T_{0i}	4
7	Identified T_r , T_{02} , and w_2 after shift	4
8	Twenty tracks: Top: melt pool width from analytical model and FEM. Bottom: analytical T_{0i}	4
List o	f Tables	
- 1	Parameter values	4